Two- and three-dimensional simulations of ultrasonic propagation through human breast tissue

T. Douglas Mast*

Applied Research Laboratory, The Pennsylvania State University, University Park, Pennsylvania 16802

Abstract: Simulations of spherical-wave ultrasonic pulse propagation through human breast tissue are presented. Breast tissue models were created by processing of volumetric photographic data from the Visible Woman project. Tissue types were empirically mapped to hue, saturation, and value parameters of the photographic data; acoustic parameters of tissue were then mapped using empirical linear relationships between mass density, sound speed, and ultrasonic absorption. Computations of ultrasonic propagation were performed in two and three dimensions using a *k*-space method incorporating tissue-dependent absorption and absorbing boundary layers. The results show wavefront distortion effects similar to measurements on breast tissue. Statistically, wavefront distortion is significantly more severe for the three-dimensional simulations than for the two-dimensional simulations.

PACS numbers: 43.80.Gx, 43.80.Qf, 43.20.Fn

Date received: 18 August 2001 Date accepted: 15 November 2001

Introduction

Direct simulation of ultrasound-tissue interaction is becoming a widespread tool for studies of ultrasonic imaging and therapy.[1–3] Increases in computational power have made possible simulations of large-scale models incorporating realistic tissue structure and direct numerical solutions to the model equations. Propagation problems of interest in medical ultrasound typically employ transient pulses and domains that span tens to hundreds of wavelengths, so that large computational grids and fine temporal resolution are required. For these reasons, most previous investigations of ultrasonic propagation through tissue have employed two-dimensional tissue models, which present small computation and storage requirements compared to three-dimensional problems.[4] One notable exception is a recent three-dimensional simulation of kHz-frequency ultrasound propagation for a realistic model of dolphin hearing.[5] Although previous models exist for three-dimensional ultrasonic propagation through random-medium models of human tissue, these have generally relied on simplifying assumptions such as weak scattering approximations[6] or axisymmetric propagation.[7] The present study presents and analyzes new three-dimensional simulations as well as corresponding two-dimensional simulations of full-wave, MHz-frequency ultrasonic propagation through breast tissue continuum models.

Breast Tissue Model

To obtain realistic three-dimensional (3D) models of human breast tissue, volumetric image data was employed. The data set chosen was from the Visible Woman project, which includes 3D x-ray computed tomography (CT), magnetic resonance imaging (MRI), and photographic data for an entire female cadaver. This data set is publicly available and has been extensively studied.[8] Although computed tomography data provide a firm basis for volumetric models of acoustic properties,[5] and similar modeling may be possible using MRI data, the CT and MRI data from the Visible Woman data set are of insufficient (about 1 mm) resolution for simulations of MHz-frequency ultrasonic propagation. The volumetric photographic data, which were obtained by photographing the cadaver layer-by-layer, have a uniform voxel size of $(1/3\ \text{mm})^3$, which was

*Current address: Ethicon Endo-Surgery, 4545 Creek Rd. ML 40, Cincinnati, OH 45242 (dmast@eesus.jnj.com)

judged adequate for the present simulations.

To map the photographic data to tissue properties, an empirical continuum model was developed. This model defines fractional fatty, connective, and parenchymal tissue content for each voxel, with the fractions always summing to 1. The segmentation rules were based on manual sampling of hue, saturation, and value (HSV) parameters of the photographic data for image regions seen to contain fatty, connective, and parenchymal (glandular) tissue. First, to reduce slice-to-slice variations due to artifacts of lighting and cut quality, the HSV maps of each slice were normalized so that their mean values matched the mean HSV values for the a group of surrounding slices. Based on empirical examination of slice-to-slice variations in HSV values, the length of this region was chosen to be 17 slices (5.67 mm). The segmentation rules were then applied in order, as follows, where H, S, and V are hue, saturation, and value maps bounded by 0 and 1, and W, P, and C are local fractions of water, parenchymal tissue, and connective tissue. (The remaining fraction is taken to be fat.)

1. Mark exterior by hue and value: $W = 1 - [u(0.4 - H) + u(H - 0.8)] + u(0.1 - V)$.
2. Mark parenchyma based on value: $P = (1 - W)\, u(0.67 - V)$.
3. Mark connective tissue based on saturation: $C = (1 - W)\, u(S - 0.45) - P$. (Set to zero where $C < 0$.)
4. Compute sound-speed map: $c = c_F + (c_0 - c_F)W + (c_P - c_F)P + (c_C - c_F)C$.

In the above algorithm, u is a smoothed step function defined as

$$u(x) = \begin{cases} 0.5 - 0.5\cos[\pi(x+\epsilon)/(2\epsilon)] & (-\epsilon < x < \epsilon), \\ 0, \quad (x < -\epsilon), \quad 1 \quad (x > \epsilon), \end{cases} \tag{1}$$

where the parameter ϵ was 0.1. Use of $u(x)$ rather than a Heaviside step function causes homogeneous regions (in which one of the tissue fractions is 1) to be connected by smooth transitions, reducing artifactual scattering from discontinuous boundaries. The sound speed values employed were, in mm/μs, $c_F = 1.478$ (fat), $c_0 = 1.524$ (water), $c_P = 1.547$ (parenchymal), and $c_C = 1.613$ (connective). Values of mass density and absorption were determined using empirical linear relations[5,9] based on fits to nominal tissue parameter values:[1,10]

$$\rho = 1.43\, c - 1.18, \quad \alpha = 0.71\, c - 1.01, \tag{2}$$

where the mass density ρ is in g/cm^3 and the (frequency-independent) absorption α, estimated for the center frequency of 2.5 MHz, corresponds to that defined by Mast *et al.*[10] The corresponding absorption in dB/mm is approximately $20\, \log_{10}(e) \times \alpha/(2c)$.

Although the resulting volumetric maps are likely not to be as accurate as maps determined from CT data[5] or as manually segmented maps,[1,10] the tissue maps obtained using the rules described above were judged sufficiently realistic for the present simulations. As shown below, the maps produce distortion comparable to measurements on breast tissue specimens.

Computational Methods

Spherical-wave pulse propagation through the breast tissue models were computed using the k-space method.[4] This method directly solves the second-order linear acoustic wave equation for media with variable sound speed and density and allows high accuracy to be obtained using relatively large temporal and spatial steps compared to other numerical methods.[4,11] Tissue-dependent absorption was incorporated using the Maxwell solid model described by Mast *et al.*,[10] which results in frequency-independent absorption. Absorbing boundary layers were incorporated using tapered absorption functions at each boundary. To minimize spurious reflections associated with absorption discontinuities,[12] the taper profile

$$\alpha(x/L) = \alpha_{\max}\,[0.375 - 0.5\cos(\pi x/L) + 0.125\cos(2\pi x/L)], \tag{3}$$

which has zero first, second, and third spatial derivatives at the edge of the absorbing layer, was chosen. In Eq. (3), x is the perpendicular distance within the absorbing layer of length L,

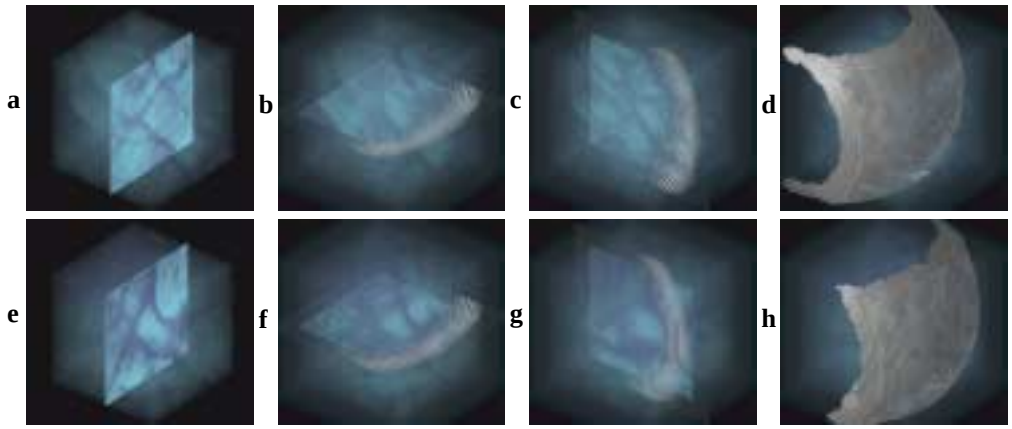

Fig. 1. Visualizations of 3D breast models and propagation. Each panel contains a translucent image of the sound speed map for the entire model volume, with cyan representing fat, medium blue representing parenchymal tissue, and dark blue representing connective tissue.
(a) Mm. 1 Fly-through rendering of breast model volume 8 (587 kb).
(b) Mm. 2 Horizontal slices of the 3D pressure field, shown on a bipolar logarithmic scale with a 65 dB dynamic range, and the sound speed map for vol. 8 (226 kb).
(c) Mm. 3 Vertical slices of pressure and sound speed for vol. 8 (244 kb).
(d) Mm. 4 Isosurface renderings of acoustic pressure for vol. 8 (587 kb).
(e) Mm. 5 Fly-through, vol. 10 (582 kb).
(f) Mm. 6 Horizontal slices, vol. 10 (227 kb).
(g) Mm. 7 Vertical slices, vol. 10 (235 kb).
(h) Mm. 8 Isosurface renderings, vol. 10 (231 kb).

taken here to be 20 pixels (2.22 mm), and $\alpha_{\max}$ is the maximum absorption coefficient within the layer, taken to be 16. This absorbing layer results, for the pulse employed here, in reflection and transmission coefficients of about -52 dB. Otherwise, the *k*-space method employed was as described by Mast *et al.*[4]

Fourteen cubic volumes of breast tissue, each containing 60^3 voxels, or $(20\ \text{mm})^3$, were modeled from the Visible Woman data using the segmentation method described above. Fourier interpolation, performed simultaneously with a Gaussian low-pass filtering operation, was used to oversample the segmented volumes by a factor of three in each direction, so that the inhomogeneous region of the grid spanned 180^3 voxels. Computations were then performed on a $240 \times 240 \times 240$ grid (240×240 for the 2D case) with a uniform voxel size of 0.111 mm. A spherical-wave source was simulated by adding the source distribution

$$q(\mathbf{r}, t) = e^{-|\mathbf{r}-\mathbf{r}_0|^2/(2\sigma_r^2)}\, e^{-(t-t_0)^2/(2\sigma_t^2)}\, \sin(2\pi f_0 t) \tag{4}$$

to the wavefield at each time step, where the source position $\mathbf{r}_0$ was centered at a position 0.7 mm below the lower boundary of the inhomogeneous region, the spatial Gaussian parameter σ_r was 0.1 mm, the temporal Gaussian parameter σ_t was 0.5 μs, and the center frequency f_0 was 2.5 MHz. (Use of a finite source size ensured isotropic propagation without any artifacts associated with the discrete Fourier transforms employed.) A time step of 0.0364 μs (corresponding to a Courant-Friedrichs-Lewy number $c_0 \Delta t / \Delta x = 0.5$, appropriate for the present *k*-space method[4]) was employed in all cases. On an 650 MHz Athlon workstation with 768 MB of random-access memory, each 3D computation took about 3.2 h.

Simulated wavefields were received by an 18×18 element aperture, with square elements at a pitch of 0.72 mm, centered 0.8 mm above the upper boundary of the inhomogeneous region. Waveforms for each simulated element were computed by integration of the received pressure with a step size of 0.18 mm (four points per simulated element). The pressure at each point of integration was determined using an accurate sinc-Kaiser interpolation method. [4]

Table 1: Wavefront distortion statistics for 3D and 2D simulations using 14 breast model volumes. Shown are the mean rms arrival time fluctuations (ATF), rms energy level fluctuations (ELF), and waveform similarity factors (WSF) for each volume, as well as overall means μ and standard deviations σ for each statistic. Volumes containing significant fractions of parenchymal tissue are denoted by asterisks.

Vol.	3D rms ATF (ns)	3D rms ELF (dB)	3D WSF	2D rms ATF (ns)	2D rms ELF (dB)	2D WSF
1	74.2	2.74	0.840	50.8	2.07	0.930
2*	56.8	1.85	0.946	45.7	1.48	0.962
3	64.0	2.55	0.920	35.6	1.44	0.969
4*	40.0	1.64	0.931	28.4	1.09	0.977
5	74.2	2.74	0.840	43.9	2.39	0.911
6*	46.8	1.95	0.943	31.1	1.29	0.971
7*	42.8	1.94	0.943	35.5	1.22	0.971
8*	85.2	3.59	0.881	42.4	1.82	0.945
9*	73.3	1.90	0.938	70.3	1.43	0.961
10	96.7	4.44	0.789	81.7	3.52	0.888
11*	65.0	2.38	0.920	42.6	1.46	0.966
12	58.5	2.31	0.872	42.9	2.10	0.939
13	84.6	3.75	0.876	58.7	2.09	0.950
14	50.2	2.01	0.893	69.6	2.13	0.938
$\mu \pm \sigma$	65.2 ± 17.1	2.56 ± 0.83	0.895 ± 0.048	48.5 ± 15.9	1.82 ± 0.64	0.949 ± 0.026

The received waveforms were analyzed for wavefront distortion effects using previously established methods.[13] Before processing, wavefields were compensated for geometric delay and amplitude variations. Arrival time fluctuations were computed by cross-correlation of each waveform with a reference waveform obtained by summing all waveforms in the aperture after geometric compensation. The peak of each cross-correlation function was found from the zero crossing of the derivative of the cross-correlation envelope, computed using second-order accurate finite differences. Waveforms were then compensated for the computed arrival time fluctuations and Hanning windowed (window length 5.8 μs). Energy level fluctuations were computed from the squared sum of each waveform in dB units. To account for any effects due to element directivity, distortion maps from an analogous computation in a homogeneous medium were subtracted from the computed maps. A waveform similarity factor[13] was also computed: this factor is a generalized cross-correlation coefficient that is equal to 1 when all waveforms in the aperture are identical.

To allow comparison of distortion effects for 2D and 3D propagation, 2D computations were carried out 18 times for each cubic inhomogeneity, corresponding to the 18 elevation positions of the receiving array from the 3D computations. All other processing was identical for the 2D cases, except that geometric corrections were based on the 2D geometry and average arrival time and energy level fluctuations for each elevation were removed before statistical evaluation.

Results

Example breast tissue maps and propagation animations are shown in Fig. 1 for two representative model volumes. Panels (a) and (e) show fly-through animations of the sound-speed maps, whereas the other panels show three different renderings of the simulated propagation. Each of the propagation animations shows the cumulative development of arrival time, energy level, and waveform distortion as wavefronts interact with inhomogeneities in the breast tissue. Volume 8 contains a mixture of fat, connective tissue, and parenchyma, and the propagation animations show large-scale arrival-time distortion as well as some waveform and energy-level distortion. Volume 10, which contains mainly fat and denser connective tissue, produces more severe waveform and energy-level distortion due to interference between the main wavefront and waves scattered by connective tissue structures.

Computed 2D and 3D wavefront distortion statistics for the 14 model volumes are shown in Table 1 and summarized in Fig. 2. These statistics indicate that, for a given medium

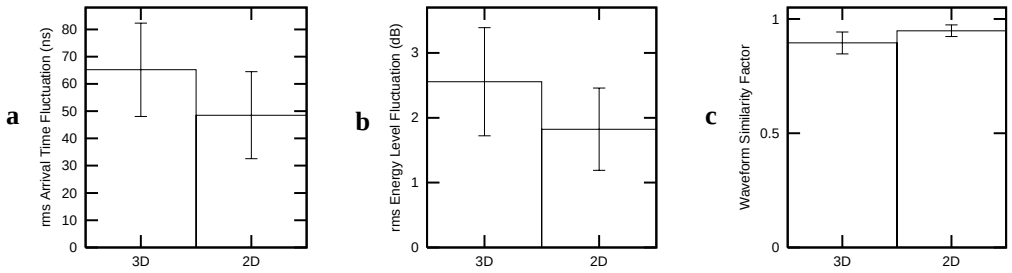

Fig. 2. Summarized distortion statistics for 3D and 2D computations using 14 model breast volumes. The box heights represent the means of each statistic whereas the error bars span ±1 standard deviation. (a) rms arrival time fluctuations, (b) rms energy level fluctuations, (c) waveform similarity factors.

model, 3D propagation produces significantly more wavefront distortion than 2D propagation. Student's *t*-test, applied to determine the probability of identical means for the 2D and 3D distortion statistics, yields $p = 6.69 \times 10^{-3}$ for the arrival time fluctuations, $p = 7.49 \times 10^{-3}$ for the energy level fluctuations, and and $p = 7.79 \times 10^{-4}$ for the waveform similarity factor. Thus, statistically significant differences between 2D and 3D propagation exist for all the distortion metrics investigated, and this difference is most significant for the waveform similarity factor.

The distortion seen for the 3D simulations qualitatively agrees with previous measurements of wavefront distortion caused by breast tissue *in vitro*. Mean distortion statistics found by Hinkelman *et al.* for 9 breast specimens included a mean rms arrival time fluctuation of 66.8 ns, a mean rms energy level fluctuation of 5.03 dB, and a mean waveform similarity factor of 0.910. [14] The statistics are not expected to be precisely comparable, however, since the experiments of Hinkelman *et al.* employed a higher-frequency, wider-band pulse (center frequency 3.75 MHz, −6 dB bandwidth 2.2 MHz) than the simulations reported here.

Discussion

The continuum tissue model introduced here was based on three-dimensional photographic data. Although the 3D computations employing this model produce realistic propagation effects, comparable to measured wavefront distortion, the subjectivity required to establish the tissue-mapping rules is a disadvantage. Alternative imaging methods such as 3D x-ray computed tomography produce volumetric data quantitatively related to tissue properties. [5] Model development using 3D CT has proven useful in lower-frequency simulations of propagation through mammalian tissue[5] and, given sufficiently high spatial resolution, would be ideal for models of ultrasonic propagation. In addition, the empirical linear relationships employed here [Eq. (2)] are approximations that may affect the accuracy of the results. In particular, the assumed linear relationship between absorption and sound speed is questionable, [9] although the speed-absorption trend here is consistent with some previous studies. [1] As discussed previously, [10] the assumption of frequency-independent absorption may cause the waveform similarity factor to be overestimated, but should not have a great effect on the other distortion statistics investigated.

Substantially higher distortion was observed here for the three-dimensional computation than for the two-dimensional computations. This result, consistent with established understanding of propagation through random media, [15] suggests that 3D propagation and scattering effects are important to ultrasonic wavefront distortion in tissue. These 3D effects may include spherical spreading of secondarily scattered wavefronts, interference between wavefronts propagating in multiple out-of-plane directions, and complicated 3D propagation paths not modeled in 2D simulations. The specific 3D structure of tissue, such as the convex shape of fat lobules, may also produce distortion effects not accurately modeled by 2D tissue cross-sections.

For these reasons, simulations of ultrasonic imaging and therapy that employ 2D tissue models are likely to underestimate the degrading effects of tissue on focus and image quality.

Thus, simulations of tissue-ultrasound interaction, *e.g.*, for design of improved imaging and therapy methods, should preferably be performed in 3D when possible. As 3D computations become more feasible, direct simulations of ultrasonic wavefields should become correspondingly more realistic and more useful as a basic tool for medical ultrasound research.

Acknowledgments

This research was funded by the Breast Cancer Research Program of the U.S. Army Medical Research and Materiel Command under Grant No. DAMD17-98-1-8141. Any opinions, findings, conclusions, or recommendations expressed in this publication are those of the author and do not necessarily reflect the views of the U.S. Army. Discussions with Laura Hinkelman, Leon Metlay, and Makoto Tabei are acknowledged with pleasure.

References

[1] T. D. Mast, L. M. Hinkelman, M. J. Orr, V. W. Sparrow, and R. C. Waag, "Simulation of ultrasonic pulse propagation through the abdominal wall," J. Acoust. Soc. Am. **102**, 1177–1190 (1997). [Erratum: J. Acoust. Soc. Am. **104**, 1124–1125 (1998).]

[2] G. Wojcik, B. Fornberg, R. Waag, L. Carcione, J. Mould, L. Nikodym, and T. Driscoll, "Pseudospectral methods for large-scale bioacoustic models," Proc. IEEE Ultrason. Symp. 1997, **2**, 1501–1506 (1997).

[3] I. M. Hallaj and R. O. Cleveland, "FDTD simulation of finite-amplitude pressure and temperature fields for biomedical ultrasound," J. Acoust. Soc. Am. **105**, L7–L12 (1998).

[4] T. D. Mast, L. P. Souriau, D.-L. Liu, M. Tabei, A. I. Nachman, and R. C. Waag, "A *k*-space method for large-scale models of wave propagation in tissue," IEEE Trans. Ultrason., Ferroelect., Freq. Contr. **48**, 341–354 (2001).

[5] J. L. Aroyan, "Three-dimensional modeling of hearing in *Delphinus delphis*," J. Acoust. Soc. Am. **110**, 3305–3318 (2001).

[6] E. M. G. P. Jacobs and J. M. Thijssen, "A simulation study of echographic imaging of diffuse and structurally scattering media," Ultrason. Imag. **13**, 316–333 (1991).

[7] T. Christopher, "Finite amplitude distortion-based inhomogeneous pulse echo ultrasonic imaging," IEEE Trans. Ultrason., Ferroelect., Freq. Contr. **44**, 125–139 (1997).

[8] M. J. Ackerman, "The Visible Human Project: A resource for anatomical visualization," Medinfo **9**, 1030–1032 (1998).

[9] T. D. Mast, "Empirical relationships between acoustic parameters in human soft tissues," Acoustics Research Letters Online **1**, 37–42 (2000).

[10] T. D. Mast, L. M. Hinkelman, L. A. Metlay, M. J. Orr, and R. C. Waag, "Simulation of ultrasonic pulse propagation, distortion, and attenuation in the human chest wall," J. Acoust. Soc. Am. **106**, 3665–3677 (1999).

[11] J. C. Mould, G. L. Wojcik, L. M. Carcione, M. Tabei, T. D. Mast, and R. C. Waag, "Validation of FFT-based algorithms for large-scale modeling of wave propagation in tissue," Proc. IEEE Ultrason. Symp. 1999, 1551–1556 (1999).

[12] R. Kosloff and D. Kosloff, "Absorbing boundaries for wave propagation problems," J. Comp. Phys. **63**, 363–376 (1986).

[13] D.-L. Liu and R. C. Waag, "Correction of ultrasonic wavefront distortion using backpropagation and a reference waveform method for time-shift compensation," J. Acoust. Soc. Am. **96**, 649–660 (1994).

[14] L. M. Hinkelman, D.-L. Liu, R. C. Waag, Q. Zhu, and B. D. Steinberg, "Measurement and correction of ultrasonic pulse distortion produced by the human breast," J. Acoust. Soc. Am. **97**, 1958–1969 (1995).

[15] J. M. Martin and S. M. Flatté, "Simulation of point-source scintillation through three-dimensional random media," J. Opt. Soc. Am. A **7**, 838–847 (1990).